Supplementary Materials

A compositional origin to ultralow-velocity zones

Samuel P. Brown, Michael S. Thorne, Lowell Miyagi and Sebastian Rost

The supplementary material includes the following sections.

S1. ULVZ thickness

S2. ULVZ density

S3. Double beam results

S4. ScP interaction with small-scale ULVZs

S5. Mineral physics calculations

S6. ULVZ formation

S1. ULVZ thickness

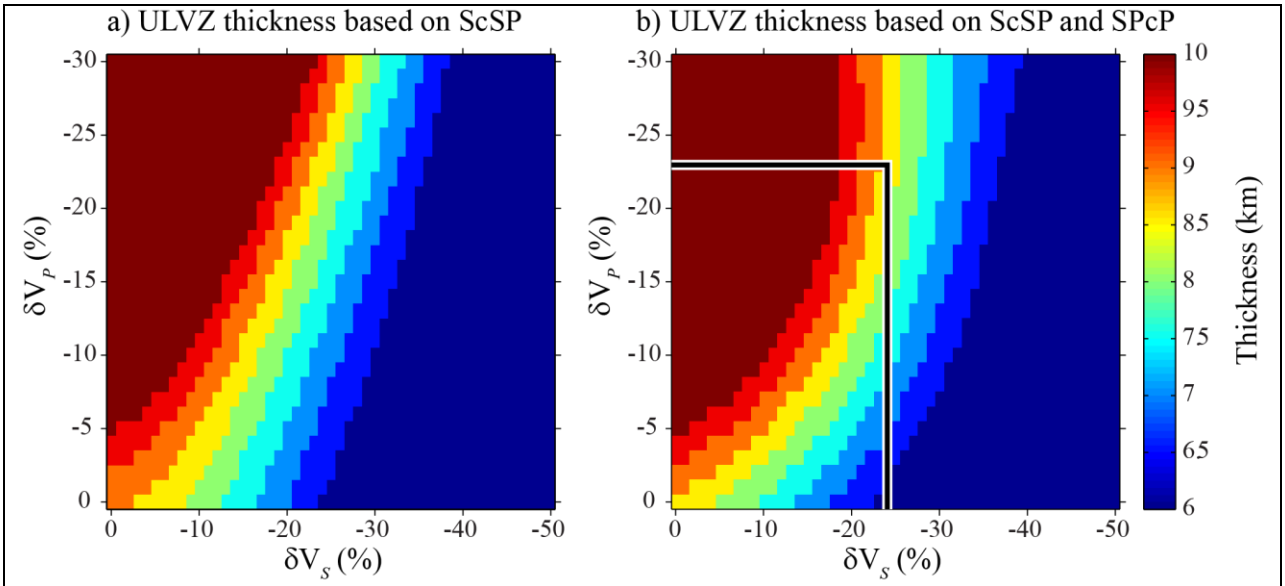

Supplemental Figure S1. a) ULVZ thicknesses associated with probabilities constrained only by ScSP travel times and amplitudes. b) ULVZ thicknesses associated with probabilities constrained by ScSP and SPcP travel times and amplitudes.

S2. ULVZ density

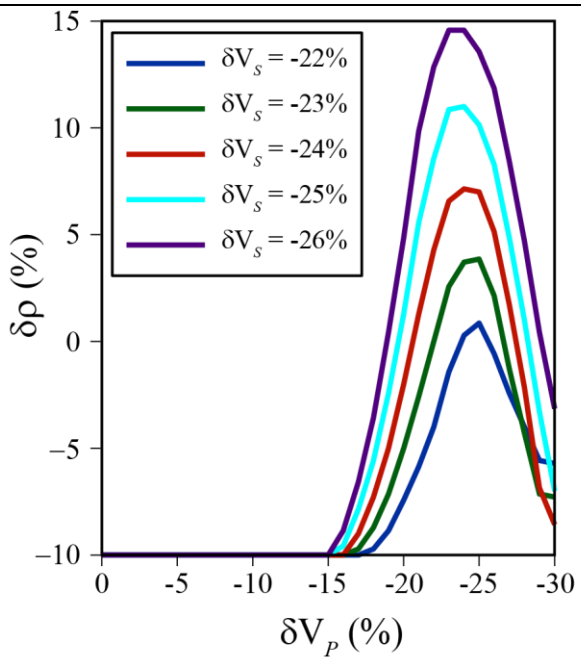

Supplemental Figure S2. Most likely density variation (δρ) as a function of P-wave velocity reduction (δV_P) for the five most likely values of S-wave velocity reduction (δV_S). S-wave velocity reductions range from -22% (blue line) to -26% (purple line).

S3. Double beam results

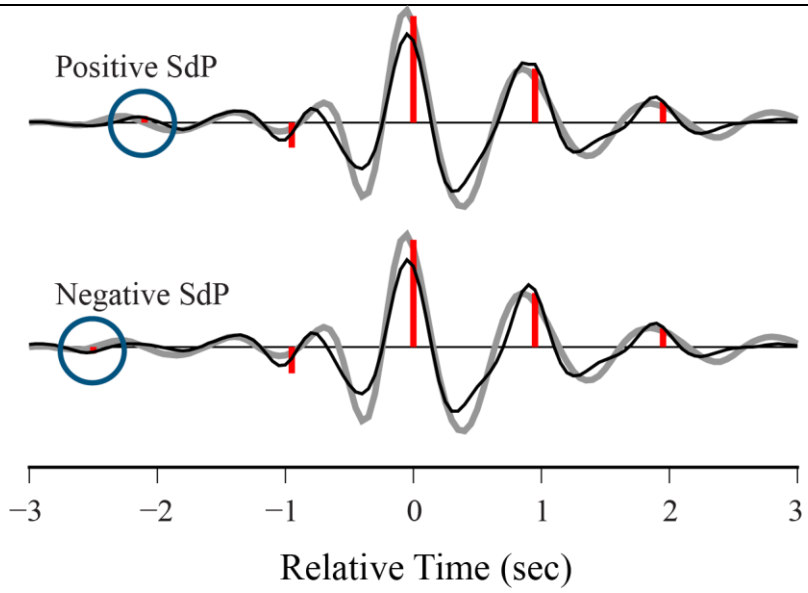

Supplemental Figure S3. Results of searching for SdP arrival in the double beam. Travel-time and amplitude picks (red spikes) computed by the VSSD method for a positive polarity SdP arrival (top trace) and for a negative polarity SdP arrival (bottom trace). The double beam formed ScP trace is shown as the gray trace. The VSSD-derived waveforms are overlain (black traces). The log-likelihood scores for the two cases are: positive = 223; and negative = 231.

S4. ScP interaction with small-scale ULVZs

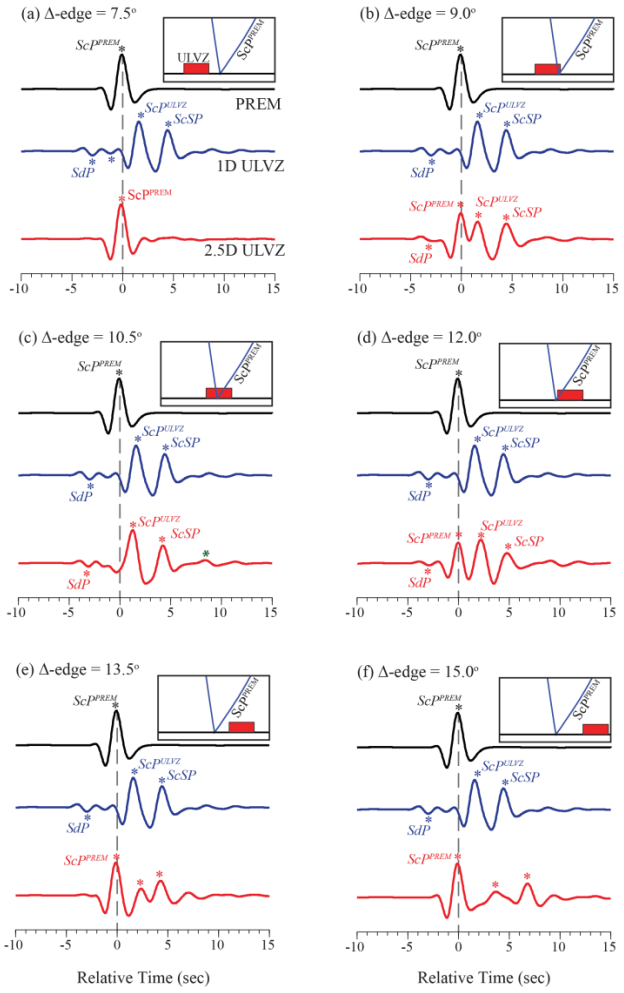

Supplemental Figure S4. Effect of ULVZ position on ScP waveforms. Each panel shows vertical component displacement waveforms normalized to unity on the largest ScP arrival in each window and aligned to the peak ScP arrival as predicted by the PREM model. In each panel the top trace (black) is the ScP waveform calculated for the PREM model. The middle trace (blue) is the ScP waveform calculated for a 1-D ULVZ model (δV_S = -30%, δV_P = -10%, $\delta\rho$ = +10%, thickness = 20 km). The bottom trace (red) is the ScP waveform calculated for a 2.5D ULVZ model. The ULVZ model has the same properties as in the middle trace, but has a length = 3.0°, and position varies in each panel from a Δ-edge location of 7.5° to 15°.

Synthetic seismograms have been computed to determine the interaction between the ScP arrival and ULVZs using a variety of techniques including the Reflectivity Method [*Fuchs and Müller*, 1971], the Direct Solution Method [*Cummins et al.*, 1997], Gaussian Beam [*Weber*, 1988], and Generalized Ray [*Helmberger*, 1983]. Thus far, these efforts have been confined to 1D models of ULVZ structure. However, interaction of the ScP arrival with small scale ULVZs may have important effects on the waveform. Our data were best fit using the VSSD method when we included an additional post-cursory arrival in the model space which is not predicted for 1D ULVZ models. In order to test the effects of small-scale ULVZs we compute a handful of high frequency synthetic seismograms using the PSVaxi technique. The PSVaxi technique utilizes axi-symmetric geometry which allows us to compute the wavefield for a 2D model, which is then virtually expanded to 3D by rotation around the axis passing through the earthquake source and the center of the Earth [see e.g., *Thorne et al.*, 2013a; *Thorne et al.*, 2013b]. This allows us to compute relatively high frequency global synthetic seismograms for a 2D input model with the correct 3D geometric spreading. Here we compute synthetic seismograms for the ScP phase at dominant periods of 3 sec. Current computational limitations do not allow calculation of synthetic seismograms at these short periods with fully 3D techniques. To date, the shortest period synthetics calculated using a full 3D method for global applications is roughly 11 sec [*Komatitsch et al.*, 2010].

1D ULVZ models are calculated allowing the following ULVZ parameters to vary: (1) S-wave velocity reduction (δV_S), (2) P-wave velocity reduction (δV_P), (3) density increase ($\delta\rho$), and (4) ULVZ thickness (h). In this study we consider box-car shaped ULVZ models similar to those investigated in [*Thorne et al.*, 2013b]. In modeling 2D ULVZs we must add two additional

parameters: (5) ULVZ lateral length in the great circle arc direction (*length*), and (6) position of the ULVZ (Δ_{edge}). We define the ULVZ position as the angular distance from the earthquake source to the leading edge of the ULVZ. We compute synthetic seismograms for a 500 km source depth for (a) the PREM model, (b) a 1-D ULVZ (δV_S = -30%, δV_P = -10%, $\delta\rho$ = +10%, thickness = 20 km), and (c) a series of 2D ULVZs (elastic parameters and thickness the same as in the case of the 1D ULVZ) with a length of 3° (~180 km along the CMB) and variation in position: $7.5° \leq \Delta_{edge} \leq 15.0°$.

Example synthetic seismograms of these calculations are shown in Supplemental Figure S4. Each panel of Fig. S4 shows the PREM synthetic seismogram at an epicentral distance of 42° (top black trace in each panel). For reference, this PREM synthetic seismogram is repeated in each panel. For the PREM synthetic seismogram we see a single arrival which we refer to as ScP^{PREM}. The middle trace of each panel (middle blue trace) is calculated for the 1D ULVZ model (this trace is also repeated in each panel for reference). Here we see the standard arrivals associated with a ULVZ (see Fig. 1c), however the ScP arrival is delayed with respect to the PREM prediction and we thus refer to this arrival as ScP^{ULVZ}. The lower trace (red trace) in each panel is the synthetic seismogram for the 2.5D ULVZ model. In the upper right corner of each panel the position of the ULVZ is shown with respect to the ScP ray path. In panel (a) the 2.5D ULVZ synthetic is shown where the ULVZ is at a position Δ_{edge} = 7.5°. In this case the down going S-wave completely misses the ULVZ and the 2.5D synthetic (red trace) looks nearly identical to the PREM prediction (black trace). In panel (b) the ULVZ is shifted to right (Δ_{edge} = 9.0°) such that the ScP ray path (here just drawn for the PREM model) is interacting with the far edge of the ULVZ. In this case ScP is multi-pathed and we see two ScP arrivals that correspond in time to ScP^{PREM} (see black trace) and ScP^{ULVZ} (see blue trace). The pre- and post-cursor

traces arrive approximately at the same time as predicted by the 1D ULVZ model. In panel (c) the ScP ray path is a direct strike on the ULVZ. Although the waveforms look slightly dissimilar, the 2.5D ULVZ synthetic (red trace) is similar in its characteristics to the 1D ULVZ synthetic (blue trace). At the other edge of the ULVZ (panel d) we see the same waveform behavior as in panel (b). As the ULVZ passes through to the other side of the ScP raypath (panels e and f) we observe a more complex waveform behavior due to the asymmetric nature of the ScP arrival. We see the ScP^{PREM} arrival as expected, but in addition see arrivals similar to ScP^{ULVZ} and ScSP. For the shorter distance (panel e) these arrivals come in at a similar time to the 1D ULVZ, but these arrivals are more delayed for the larger distance (panel e).

The primary conclusions we draw from these calculations are: (1) If the ULVZ is located at a shorter angular distance than the ScP CMB bounce point then the waveforms are similar to those predicted by the PREM model, (2) If the ScP bounce point is in the middle of the ULVZ then the waveforms are as predicted by the 1D ULVZ model, (3) If the ScP bounce point is at the edge of a ULVZ then we see complex multi-pathing and the generation of two ScP arrivals, and (4) If the ULVZ is located at a distance that is larger than the ScP bounce point some of the upgoing *P*-wave energy, which is at near grazing angles, may interact with the ULVZ and produce post-cursory arrivals. However, in this case we don't observe any precursors.

The data we examined in this study, were shown by Rost *et al.,* [2006] to exhibit arrivals that looked similar to 1D ULVZ models. Additional events showed complex multi-pathed looking waveforms which are similar to what we observe in Fig. 8 panels (b) and (d). These multi-pathed data could be marking the boundary of the ULVZ in this region. The locations of ScP bounce points in our study area are on the far side of these multi-pathed data, hence we do not believe that the post-cursors we are measuring are due to an indirect hit on the ULVZ, as Fig.

S4 panels (e) and (f) demonstrate could give rise to waveforms similar to those we analyze. Thus, we believe the data we examine in this study are due to a direct strike on the ULVZ such as is pictured in Fig. S4c. There is an additional post-cursor visible in Fig. 8c (marked with a green asterisk). The position and amplitude of this post-cursor varies depending on the exact location of the far edge of the ULVZ with respect to the ScP bounce point and likely corresponds with a diffracted arrival off the far edge of the ULVZ. Hence, if the additional post-cursor we observe in this study is due to the interaction with the far edge of this ULVZ then we could potentially measure the lateral size of the ULVZ along the CMB. Additional computation of high frequency synthetic seismograms would be necessary to complete this step and is reserved for future endeavors.

It is also important to note that previous studies examining the ScP waveforms have not considered the effects of 2- or 3D ULVZs. Hence, we caution interpretation of ULVZ position when only ScP postcursors have been examined. Absence of ScP precursors could be due to the ScP bounce point missing the ULVZ, yet a post-cursor may still be present.

S5. Mineral physics calculations

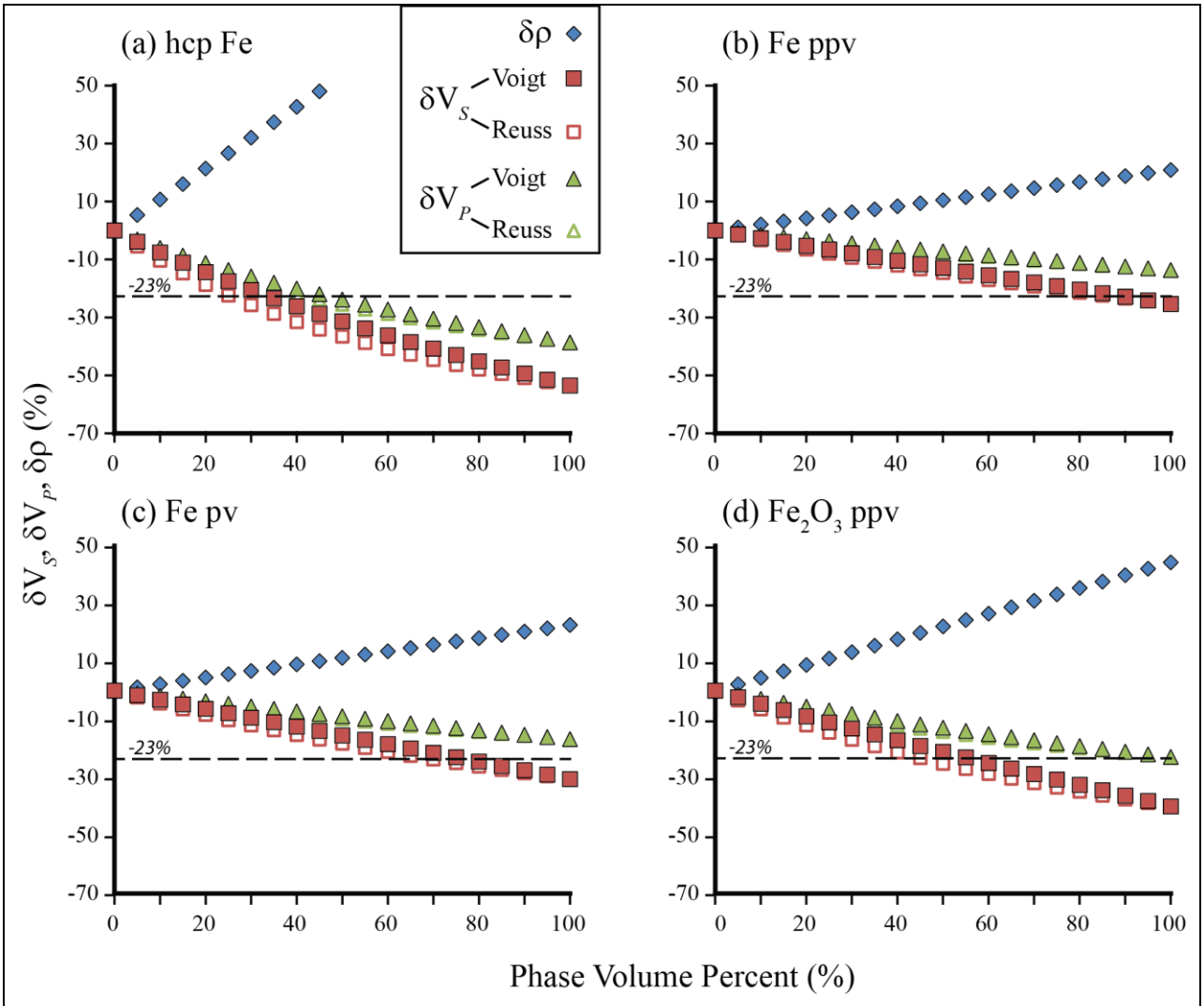

Supplemental Figure S5. Percent change in V_S, V_P, and ρ with respect to PREM for various phase proportions of (a) hcp Fe, (b) Fe-pPv, (c), Fe-Pv, and (d) Fe_2O_3 pPv mixed with PREM. Dashed line indicates the observed -23% decrease in V_S and V_P.

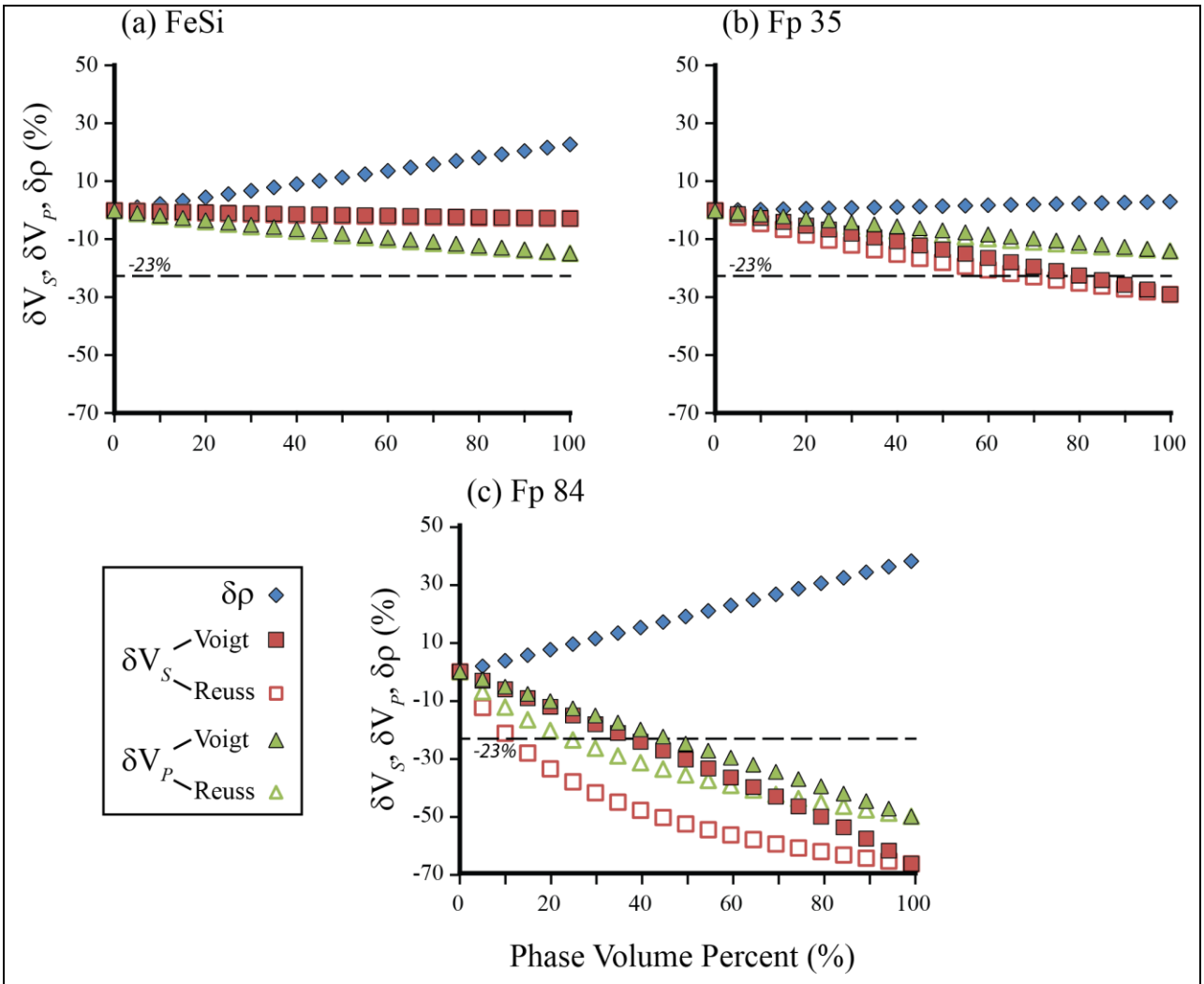

Supplemental Figure S6. Same as figure S4, but for (a) FeSi, (b) Fp 35, and (c) Fp 84.

For the calculation of seismic velocities we use a combination of experimental and theoretical literature values for shear modulus (G), bulk modulus (K) and density (ρ). In guiding our choices of mineral phases to explore, we considered that the appropriate phase not only needs to have significantly slower velocities than the Preliminary Earth Reference Model (PREM) [*Dziewonski and Anderson*, 1981] but the phase must also be significantly denser than PREM such that it can match both the velocity reduction and provide ~10% density increase

over PREM. Based on these guidelines we choose to explore Fe enrichment of silicates and oxides or the mixing of pure Fe metal or FeSi as possible sources for ultra-low velocities. Phases tested are $(Mg_{0.65},Fe_{0.35})O$ ferropericlase (Fp35), $(Mg_{0.16},Fe_{0.84})O$ ferropericlase (Fp84), $FeSiO_3$ post-perovskite (Fe-pPv), Fe_2O_3 pPv, $FeSiO_3$ perovskite (Fe-Pv), hexagonal close-packed Fe (hcp-Fe), and B2 structured FeSi.

To correct G and K to high temperature (T) we adopt a simple linear approximation. Namely,

$$G_{P,T} = G_{P,0} + \partial G/\partial T (T - T_0) \quad \text{(Eqn. S1)}$$

$$K_{P,T} = K_{P,0} + \partial K/\partial T (T - T_0) \quad \text{(Eqn. S2)}$$

where T_0 is a reference temperature, typically 298 K. Density is corrected to temperature using the following equations:

$$\rho_T = \rho_{T_0} exp - \int_{T_0}^{T} \alpha(T) \quad \text{(Eqn. S3)}$$

where

$$\alpha(T) = \alpha_0 + \alpha_1(T) \quad \text{(Eqn. S4)}$$

where α is thermal expansion and ρ is density.

For ferropericlase we use sound velocity measurements of Chen *et al.*, [2012] for Fp35, and from Wicks *et al.*, [2010] for Fp84. To extrapolate these datasets to core-mantle boundary conditions we only use data collected after the high-spin to low-spin transition. For the correction of the elastic properties of Fp35 and Fp84 to high temperature we use values from theoretical calculations for $\partial G/\partial T$ and $\partial K/\partial T$ of pure end member MgO periclase [*Karki et al.*,

2000]. Density and pressure is taken from Chen *et al.*, [2012] for Fp35 and from [*Karki and Crain*, 1998] for Fp84. Thermal expansion values of α_0 and α_1 for $(Mg_{0.64}, Fe_{0.36})O$ [*van Westrenen et al.*, 2005] were used to correct density of Fp35 and Fp84 to high temperature.

For Fe pPv and Fe_2O_3 pPv we use values of K, G and, ρ that were calculated using the generalized gradient approximation + Hubbard U (GGA+U) approach for high-spin antiferromagnetic Fe-PPv and low-spin antiferromagnetic Fe_2O_3 pPv [*Stackhouse and Brodholt*, 2008]. For Fe-pPv it is assumed that temperature derivative of elastic properties and density are identical to $MgSiO_3$ post-perovskite and thus we use $\partial G/\partial T$, $\partial K/\partial T$, and $\partial \rho/\partial T$ from Stackhouse *et. al.*, [2007] to correct K, G and ρ to high temperature. Elastic properties at high pressure and temperature for Fe-Pv are taken from Stackhouse *et al.*, [2006].

For hcp-Fe we use K, G, ρ, and $\partial G/\partial T$ derived from sound velocity measurements [*Lin et al.*, 2005]. $\partial K/\partial T$ and α at 136GPa and 3500 K were taken from Isaak and Anderson [2003]. Calculated sound velocities of Ono [2013] combined with densities from the theoretical equation of state of Caracas and Wentzcovitch [2004] were used to derive K and G for B2 structured FeSi. Caracas and Wentzcovitch [2004] show densities obtained with both local density approximation (LDA) and generalized gradient approach (GGA) and we use an average of these values for these calculations. To correct density of B2 FeSi to high temperature we approximate this with the thermal expansion coefficients for ε-FeSi [*Vočadlo et al.*, 2002].

Since the detailed mineralogical and chemical composition at the base of the mantle is uncertain, rather than attempt to model a complete mineralogical mixture, we instead perform a simple computation where the mineral phase of interest is mixed with PREM velocities and

densities. Note that this is identical to the approach adopted by Wicks *et al.*, [2010]. This has the advantage that precise mineralogical make-up of the surrounding mantle is not needed. However in some cases it may underestimate mineral phase proportion. For example for ferropericlase mixing, PREM already likely contains somewhere in the range of 20-35 volume % of Fp (with ~10% Fe) so a phase proportion of ferropericlase mixed with PREM will actually be considerably smaller that the "true" percentage of ferropericlase.

To calculate elastic properties for polyphase aggregates we calculate the Voigt [*Voigt*, 1928] and Reuss bounds [*Reuss*, 1929]:

$$M^{Voigt} = \sum_{i}^{N} f_i \, M_i \qquad \text{(Eqn. S5)}$$

$$\frac{1}{M^{Reuss}} = \sum_{i}^{N} \frac{f_i}{M_i} \qquad \text{(Eqn. S6)}$$

Where M^{Voigt} is the Voigt average of the modulus, M^{Reuss} is the Reuss average of the modulus, f_i is the volume fraction on phase *i* and M_i is the modulus of phase *i*. We use a simple volume average to calculate density of the aggregate.

$$\rho_{polyphase} = \sum_{1}^{N} f_i \rho_i \qquad \text{(Eqn. S7)}$$

Where f_i is the volume fraction of phase *i* and ρ_i is the density of phase *i*.

Figures S4 and S5 shows results for % change in V_S, V_P, and ρ with respect to PREM for mixing of the various phases tested. Only Fp84 can provide a 1:1 decrement ratio in V_S:V_P at a ~23% decrease in velocities with an ~ 10% increase in density. For very small decreases in V_S:V_P velocities Fp35 can provide a 1:1 decrease but only for velocity decreases of ~5% or less.

For most ranges of mixing the decrement ratio is closer to 2:1. Crystalline hcp-Fe can provide ~23% decrease at an ~1.5:1 decrement ratio, but the density increase is much too large, ~35%. In fact the very high density of Fe compared to mantle silicates and oxides is the main reason why incorporation of Fe decreases seismic velocities rather than elastic properties. Thus one could in principle distinguish this seismically from other models. All other phases (Fe-pPv, Fe-Pv, Fe_2O_3 pPv, and FeSi) provide an ~2:1 decrement ratio for a 23% decrease in V_S or cannot in the case of FeSi cannot provide a 23% decrement even with 100% FeSi.

S6. ULVZ formation

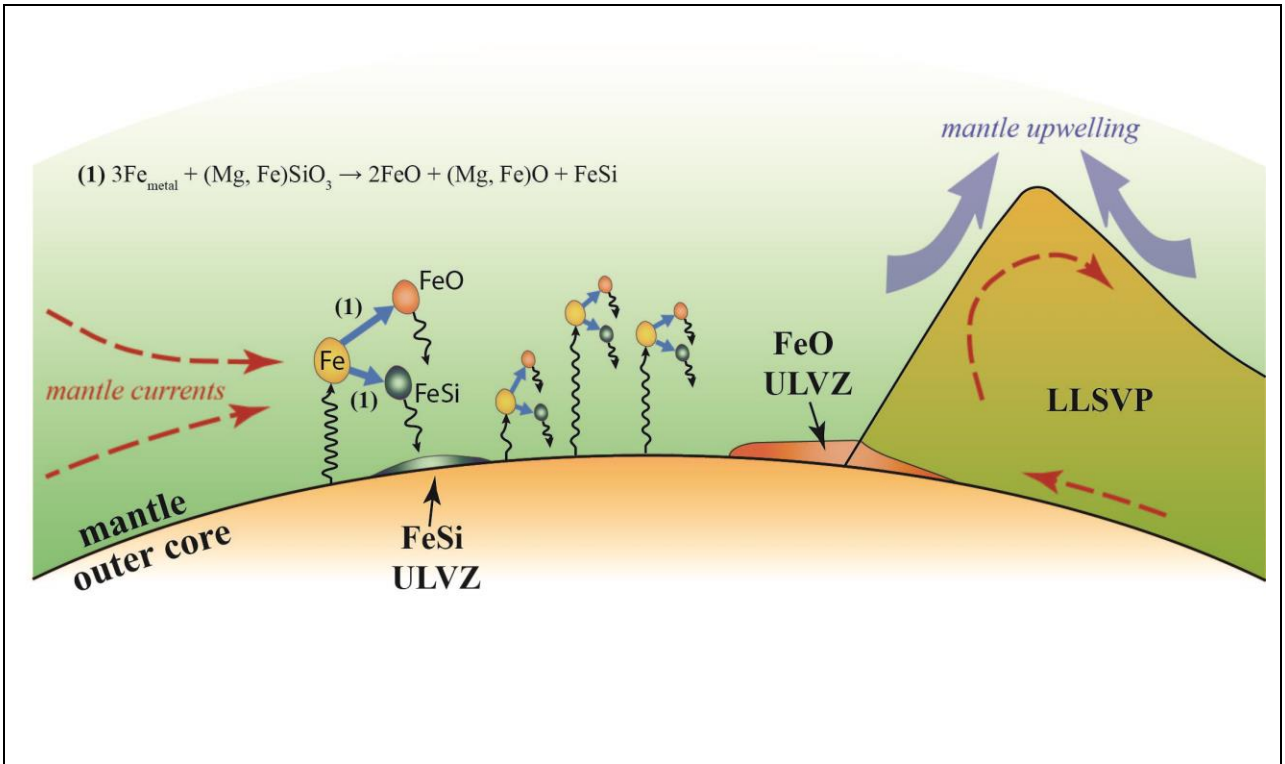

Supplemental Figure S7. Stages of ULVZ formation. Liquid Fe (yellow blobs) percolates from the outer core into the lower mantle. The reaction of liquid Fe with mantle silicates generates FeSi (green blobs) and FeO (orange blobs). FeSi and FeO are denser than ambient lower mantle and will settle to the CMB. Subsequent mantle flow concentrates FeO or FeSi into ULVZs that pile up near the margins of LLSVPs.

References

Caracas, R., and R. M. Wentzcovitch (2004), Equation of state and elasticity of FeSi, *Geophys. Res. Lett.*, *31*(L20603), doi: 10.1029/2004GL020601.

Chen, B., J. M. Jackson, W. Sturhahn, D. Zhang, J. Zhao, J. K. Wicks, and C. A. Murphy (2012), Spin crossover equation of state and sound velocities of $(Mg_{0.65}Fe_{0.35})O$ ferropericlase to 140 GPa, *J. Geophys. Res.*, *117*(B08208), doi: 10.1029/2012JB009162.

Cummins, P. R., N. Takeuchi, and R. J. Geller (1997), Computation of complete synthetic seismograms for laterally heterogeneous models using the Direct Solution Method, *Geophys. J. Int.*, *130*, 1-16.

Dziewonski, A. M., and D. L. Anderson (1981), Preliminary reference Earth model, *Phys. Earth Planet. Inter.*, *25*, 297-356.

Fuchs, K., and G. Müller (1971), Computation of Synthetic Seismograms with the Reflectivity Method and Comparison with Observations, *Geophys. J. Roy. Astron. Soc.*, *23*, 417-433.

Helmberger, D. V. (1983), Theory and application of synthetic seismograms, in *Earthquakes: Observation, Theory and Interpretation*, edited by H. Kanamori, pp. 173-222, Soc. Ital. di Fis., Bologna, Italy.

Isaak, D. G., and O. L. Anderson (2003), Thermal expansivity of HCP iron at very high pressure and temperature, *Physica B: Condensed Matter*, *328*, 345-354, doi: 10.1016/S0921-4526(02)01858-6.

Karki, B. B., and J. Crain (1998), First-principles determination of elastic properties of $CaSiO_3$ perovskite at lower mantle pressures, *Geophys. Res. Lett.*, *25*(14), 2741-2744.

Karki, B. B., R. M. Wentzcovitch, S. de Gironcoli, and S. Baroni (2000), High-pressure lattice dynamics and thermoelasticity of MgO, *Physical Review B*, *61*(13), 8793-8800, doi: 10.1103/PhysRevB.61.8793.

Komatitsch, D., L. P. Vinnik, and S. Chevrot (2010), SHdiff-SVdiff splitting in an isotropic Earth, *J. Geophys. Res.*, *115*(B07312), doi: 10.1029/2009JB006795.

Lin, J.-F., W. Sturhahn, J. Zhao, G. Shen, H.-k. Mao, and R. J. Hemley (2005), Sound Velocities of Hot Dense Iron: Birch's Law Revisited, *Science*, *308*, 1892-1894, doi: 10.1126/science.1111724.

Ono, S. (2013), Equation of state and elasticity of B2-type FeSi: Implications for silicon in the inner core, *Phys. Earth Planet. Inter.*, *224*, 32-37, doi: 10.1016/j.pepi.2013.08.009.

Reuss, A. (1929), Berechnung der Fließgrenze von Mischkristallen auf Grund der Pastizitätsbedingung für Einkristalle, *Journal of Applied Mathematics and Mechanics*, *9*(1), 49-58, doi: 10.1002/zamm.19290090104.

Rost, S., E. J. Garnero, and Q. Williams (2006), Fine-scale ultralow-velocity zone structure from high-frequency seismic array data, *J. Geophys. Res.*, *111*(B09310), doi: 10.1029/2005JB004088.

Stackhouse, S., and J. P. Brodholt (2008), Elastic properties of the post-perovskite phase of Fe_2O_3 and implications for ultra-low velocity zones, *Phys. Earth Planet. Inter.*, *170*, 260-266, doi: 10.1016/j.pepi.2008.07.010.

Stackhouse, S., J. P. Brodholt, and G. D. Price (2006), Elastic anisotropy of $FeSiO_3$ end-members of the perovskite and post-perovskite phases, *Geophys. Res. Lett.*, *33*(L01304), doi: 10.1029/2005GL023887.

Stackhouse, S., J. P. Brodholt, and G. D. Price (2007), Electronic spin transitions in iron-bearing $MgSiO_3$ perovskite, *Earth Planet. Sci. Lett.*, *253*, 282-290, doi: 10.1016/j.epsl.2006.10.035.

Thorne, M. S., Y. Zhang, and J. Ritsema (2013a), Evaluation of 1D and 3D seismic models of the Pacific lower mantle with S, SKS, and SKKS traveltimes and amplitudes, *J. Geophys. Res.*, *118*, 1-11, doi: 10.1002/jgrb.50054.

Thorne, M. S., E. J. Garnero, G. Jahnke, H. Igel, and A. K. McNamara (2013b), Mega Ultra Low Velocity Zone and Mantle Flow, *Earth Planet. Sci. Lett.*, *364*, 59-67, doi: 10.1016/j.epsl.2012.12.034.

van Westrenen, W., et al. (2005), Thermoelastic properties of $(Mg_{0.64}Fe_{0.36})O$ ferropericlase based on in situ X-ray diffraction to 26.7 GPa and 2173 K, *Phys. Earth Planet. Inter.*, *151*, 163-176, doi: 10.1016/j.pepi.2005.03.001.

Vočadlo, L., K. S. Knight, G. D. Price, and I. G. Wood (2002), Thermal expansion and crystal structure of FeSi between 4 and 1173 K determined by time-of-flight neutron powder diffraction, *Phys. Chem. Minerals*, *29*(2), 132-139, doi: 10.1007/s002690100202.

Voigt, W. (1928), *Lehrbuch der kristallphysik*, B.G. Teubner, Leipzig.

Weber, M. (1988), Computation of body-wave seismograms in absorbing 2-D media using the Gaussian beam method: comparison with exact methods, *Geophys. J. Int.*, *92*, 9-24.

Wicks, J. K., J. M. Jackson, and W. Sturhahn (2010), Very low sound velocities in iron-rich (Mg,Fe)O: Implications for the core-mantle boundary region, *Geophys. Res. Lett.*, *37*(L15304), doi: 10.1029/2010GL043689.